Extraordinary Enhancement of Quadrupolar Transitions Using Nanostructured Graphene

Stephen Sanders,[†] Asher May,[†] Alessandro Alabastri,[‡] and Alejandro Manjavacas*,[†]

†Department of Physics and Astronomy, University of New Mexico, Albuquerque, New Mexico 87131, United States

‡Department of Physics and Astronomy and Department of Electrical and Computer Engineering, Rice University, 6100 Main Street, Houston, Texas 77005, United States

E-mail: manjavacas@unm.edu

Abstract

Surface plasmons supported by metallic nanostructures interact strongly with light and confine it into subwavelength volumes, thus forcing the corresponding electric field to vary within nanoscale distances. This results in exceedingly large field gradients that can be exploited to enhance the quadrupolar transitions of quantum emitters located in the vicinity of the nanostructure. Graphene nanostructures are ideally suited for this task, since their plasmons can confine light into substantially smaller volumes than equivalent excitations sustained by conventional plasmonic nanostructures. Furthermore, in addition to their geometric tunability, graphene plasmons can also be efficiently tuned by controlling the doping level of the nanostructure, which can be accomplished either chemically or electrostatically. Here, we provide a detailed investigation of the enhancement of the field gradient in the vicinity of different graphene nanostructures. Using rigorous solutions of Maxwell's equations, as well as an analytic

electrostatic approach, we analyze how this quantity is affected by the size, shape, doping level, and quality of the nanostructure. We investigate, as well, the performance of arrays of nanoribbons, which constitute a suitable platform for the experimental verification of our predictions. The results of this work bring new possibilities to enhance and control quadrupolar transitions of quantum emitters, which can find application in the detection of relevant chemical species, as well as in the design of novel light emitting devices.

Keywords

Graphene nanostructures, graphene plasmons, electric field gradient, quadrupolar transitions, dipole-forbidden, near field.

The interaction between light and quantum emitters such as atoms, molecules, and quantum dots, is ultimately governed by the coupling of their constituent charges with the electromagnetic field. Taking into account that the dimensions of quantum emitters are usually much smaller than the wavelength of light, this coupling can be conveniently described using the multipolar light-matter interaction Hamiltonian^{1,2}

$$\mathcal{H} = -\mathbf{p} \cdot \mathbf{E} - \mathbf{m} \cdot \mathbf{B} - \mathbf{Q} : \nabla \mathbf{E} + \dots$$
 (1)

Here, **E** and **B** are the electric and magnetic fields, while **p**, **m**, and **Q** represent the electric dipole, the magnetic dipole, and the electric quadrupole moments of the quantum emitter. Importantly, as opposed to **p** and **m**, which are vectorial quantities, **Q** is a tensor, and therefore the double dot product in Eq. (1) is defined as **Q**: $\nabla \mathbf{E} = \sum_{ij} Q_{ij} \partial_i E_j$, with $\partial_i = \partial/\partial r_i$. The components of these moments are defined in terms of the charge $\rho(\mathbf{r})$ and current $\mathbf{J}(\mathbf{r})$ densities of the quantum emitter as (notice we use Gaussian units) $p_i = \int r_i \rho(\mathbf{r}) d\mathbf{r}$, $m_i = \frac{1}{2c} \int [\mathbf{r} \times \mathbf{J}(\mathbf{r})]_i d\mathbf{r}$, and $Q_{ij} = \frac{1}{6} \int (3r_i r_j - r^2 \delta_{ij}) \rho(\mathbf{r}) d\mathbf{r}$, respectively.³

The rate of a transition between two states of a quantum emitter, induced by the light-

matter interaction Hamiltonian, can be calculated using Fermi's golden rule⁴ as

$$\Gamma = \frac{2\pi}{\hbar} \left| \langle f | \mathcal{H} | i \rangle \right|^2 \delta \left(\epsilon_{fi} - \hbar \omega \right), \tag{2}$$

where $|i\rangle$ and $|f\rangle$ represent the initial and final states, ϵ_{fi} is the energy difference between the two states, and ω is the frequency of the electromagnetic field. Examining Eqs. (1) and (2), it is clear that, while transitions mediated by electric and magnetic dipole moments are controlled, respectively, by the electric and magnetic field at the position of the quantum emitter, transitions involving the electric quadrupole are proportional to the gradient of the electric field. Therefore, for a quantum emitter excited by a plane wave of amplitude E_0 , the rates of electric and magnetic dipole transitions are, respectively, proportional to E_0^2 and $(v/c)^2 E_0^2$, where v is the velocity of the charges producing the magnetic dipole and c is the speed of light. Similarly, for an electric quadrupole transition, the corresponding rate is proportional to $(Dk)^2E_0^2$, with D being the length scale of the charge distribution associated with the quadrupole moment, and $k = \omega/c$ the light wavenumber. Usually, since $v \ll c$ and $D \ll 1/k$, most optical processes in light-matter interaction are dominated by electric dipole transitions, while magnetic dipole, electric quadrupole, and higher order transitions are usually termed as forbidden, due to their significantly weaker character. However, dipoleforbidden transitions play an important role in the photochemistry and spectroscopy of many relevant chemical species, including individual atoms⁵⁻⁹ and homonuclear diatomic molecules, as well as other molecules with high symmetry, such as carbon dioxide, methane, and benzene. 10-14

One way to increase the rates of forbidden transitions is by exploiting the large field enhancement provided by the localized surface plasmons supported by metallic nanostructures. ^{15,16} These excitations couple strongly with light, confining it in volumes much smaller than its wavelength. ¹⁷ As a consequence, the electric field near the nanostructure can be a few orders of magnitude larger than that used to excite the plasmon resonance, ¹⁸ which has

already been exploited to achieve ultrasensitive biosensensing $^{19-26}$ and efficient nanoscale light emission. $^{27-30}$ The same mechanism leads to extraordinary magnetic fields in the vicinity of the metallic nanostructure, $^{31-33}$ which can be used to increase the rates of magnetic dipole transitions, $^{34-39}$ such as the singlet to triplet transition in molecular oxygen. 40,41

Another consequence of the large field confinement provided by surface plasmons is that the electromagnetic field is forced to rapidly vary within a length scale comparable to or smaller than the nanostructure size. This means that the electric field gradient near the nanostructure can be much larger than that of a plane wave, which is proportional to kE_0 . Therefore, the surface plasmons supported by the nanostructure are expected to enhance the rate of an electric quadrupole transition of a nearby quantum emitter by a factor of the order $(kD)^{-2}$, that is, proportional to the mismatch between the nanostructure size D and the transition wavelength $\lambda = 2\pi/k$. This effect has been explored using different metallic structures, including surfaces, ⁴³ cavities, ⁴⁴ slits, ⁴⁵ nanoparticle dimers ^{46–48} and arrays, ⁴⁹ as well as nanotips, ^{50–52} to cite some.

The recent emergence of graphene as a plasmonic material has brought new alternatives to enhance light-matter interactions. $^{53-55}$ Finite nanostructures carved out of graphene sheets support plasmon resonances that confine light into substantially smaller volumes than equivalent excitations sustained by conventional plasmonic nanostructures. $^{56-60}$ Therefore, they enable a much larger mismatch between the wavelength of light and the nanostructure size, which is expected to result in extraordinary electric field gradients. Furthermore, graphene plasmons can be efficiently tuned by controlling the doping level of the nanostructure, which can be accomplished in an active manner via electrostatic gating, $^{61-63}$ thus providing an efficient mechanism to adjust the frequency of the plasmon to that of the quadrupole transition. In this context, Rivera *et al.* 64 have recently predicted that the strong field confinement provided by the surface plasmon polaritons supported by infinite graphene sheets can enhance a variety of dipole-forbidden transitions of quantum emitters placed in their vicinity. Here, we present a detailed investigation of the enhancement of the electric field gradient produced

by a variety of finite graphene nanostructures that support localized surface plasmons. Our results are obtained by rigorously solving Maxwell's equations using a finite element method (FEM) approach. Additionally, we derive a semianalytical model based on the plasmon wave function (PWF) formalism, which provides useful insights on the effect that different geometric and material parameters have on the electric field gradient. Furthermore, we analyze the performance of arrays of graphene nanoribbons, which constitute a potential platform for the experimental verification of our predictions. The results of this work help to provide new insights on the enhancement of quadrupolar transitions using finite graphene nanostructures, which can be useful to develop new applications in sensing, light emission, and quantum information processing.

Results and Discussion

We start our investigation by analyzing the simplest possible graphene nanostructure, namely a nanodisk with diameter $D=50\,\mathrm{nm}$ carved out from a single graphene monolayer, which is shown in Figure 1(a). The nanodisk is doped to a Fermi energy $E_{\mathrm{F}}=0.5\,\mathrm{eV}$, relative to the Fermi energy for the neutral structure, and its response is described through the surface conductivity σ , for which we adopt a Drude model ⁵⁵

$$\sigma(\omega) = \frac{e^2}{\pi \hbar^2} \frac{iE_F}{(\omega + i\gamma)}.$$
 (3)

This model has been shown to be accurate for nanostructures with sizes larger than ~ 10 nm, at energies $\hbar\omega < E_{\rm F}$. The conductivity and, consequently, the response of the graphene nanodisk is influenced to a great extent by the damping coefficient γ , which is determined by the material losses and fabrication imperfections of the nanostructure. This parameter is often quantified using the electron mobility, μ , as $\gamma = ev_{\rm F}^2/\mu E_{\rm F}$, where $v_{\rm F} \approx c/300$ is the Fermi velocity of graphene electrons. In this work, we assume $\hbar\gamma = 10\,{\rm meV}$ that corresponds to $\mu \approx 1300\,{\rm cm}^2/({\rm V\,s})$ for $E_{\rm F} = 0.5\,{\rm eV}$, which is a conservative value within

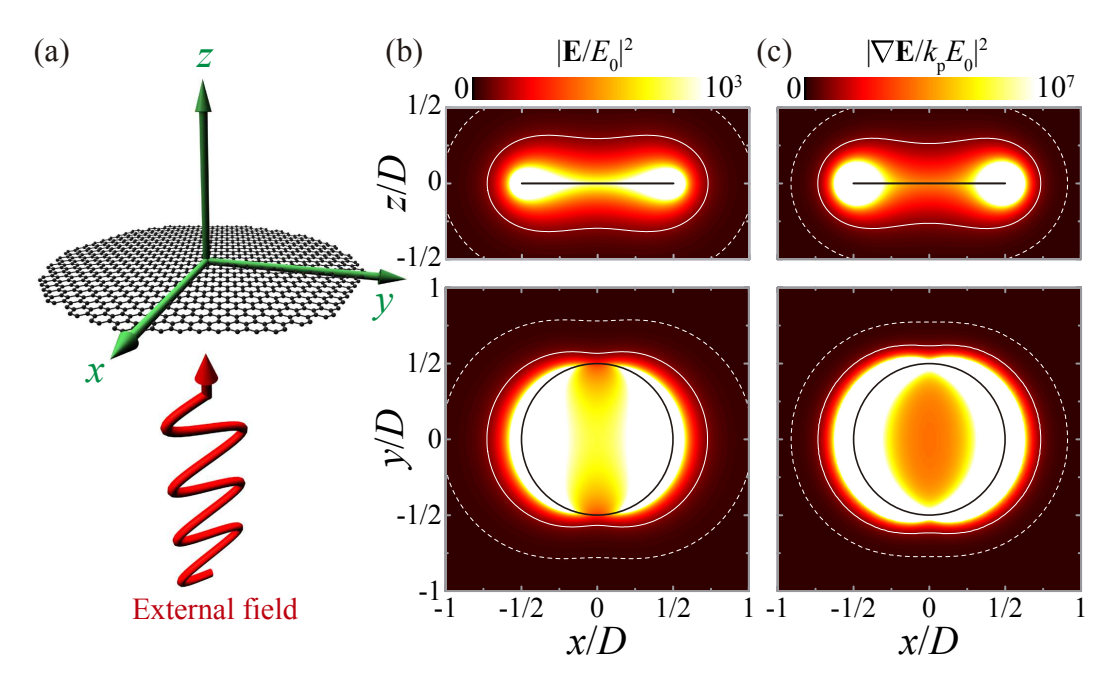


Figure 1: Near field response of a graphene nanodisk. (a) Schematics of the system under study, consisting of a graphene nanodisk of diameter $D=50\,\mathrm{nm}$ and Fermi energy $E_{\mathrm{F}}=0.5\,\mathrm{eV}$, which is illuminated with a plane wave propagating along the z axis and polarized along the x axis. Enhancement of the intensity of the field (b) and the field gradient (c), calculated at the plasmon frequency $\hbar\omega_{\mathrm{p}}=0.251\,\mathrm{eV}$. The dashed and solid white contours signal the regions for which the enhancement is larger than 10 and 100 for panel (b), and larger than 10^5 and 10^6 for panel (c). In both panels (b) and (c), the upper plot shows results for the xz plane, while the lower one displays those corresponding to a plane parallel to the nanodisk at a distance z=0.02D above it. In all cases, the solid black contour indicates the edge of the graphene nanodisk.

experimental reach.⁵⁶ Indeed, mobilities several orders of magnitude larger than that value have been measured for self-standing⁶⁵ and h-BN-encapsulated^{66,67} graphene samples.

Figure 1(b) shows the electric field intensity around the nanodisk calculated using the FEM approach (see the Supporting Information). We assume the nanostructure is illuminated with an electromagnetic field plane wave of amplitude E_0 , propagating along the zaxis and polarized along the x axis. The frequency of this field is chosen to be resonant with the frequency of the dipole plasmon supported by the nanodisk, which, for the values of Dand $E_{\rm F}$ under consideration, is $\hbar\omega_{\rm p}=0.251\,{\rm eV}$. The upper panel shows the results for the xzplane, while the lower one displays those corresponding to a plane parallel to the nanodisk a distance z = 0.02D above it. In both cases, the location of the graphene nanodisk is depicted with a black line, while the dashed and solid white contours delimit the region for which the field intensity, normalized to that of the incident plane wave, is larger than 10 and 100, respectively. These results clearly show the large field confinement generated by the surface plasmon of the graphene nanodisk. They also show the rapid variation of the near field amplitude around the nanodisk, which anticipates a very large electric field gradient. This prediction is confirmed in Figure 1(c), where we plot the field gradient intensity, defined as $|\nabla \mathbf{E}|^2 = \sum_{ij} |\partial_i E_j|^2$, normalized to that of the illuminating plane wave $|k_p E_0|^2$. The latter, as discussed before, is just the product of the wave vector of the plane wave, $k_{\rm p}=\omega_{\rm p}/c$, with its amplitude E_0 . In this case, the dashed and solid white contours indicate the regions for which the enhancement of the field gradient intensity are above 10^5 and 10^6 , respectively. These values are sufficient to bring the rate of quadrupole transitions close to that of dipole transitions. For instance, in Hydrogen, ⁶⁸ the ratio between the decay rate of the $5p \to 4s$ and the $5d \to 4s$ transitions, both of which occur at an energy $\hbar\omega = 0.306\,\mathrm{eV}$, is $\approx 1.4 \times 10^6$. The results of Figure 1(c) confirm that, despite the relatively large damping used in the calculations, enhancements above 10^5 are obtained over a volume $\approx 2D^3$ around the nanodisk, which for $D = 50 \,\mathrm{nm}$ results in a volume of $2.5 \times 10^5 \,\mathrm{nm}^3$. Comparable values of enhancement have been predicted at the gap between two metallic particles separated by a few nanometers, although, in that case, the enhancement is achieved over significantly smaller volumes localized within the gap. 42,46,47

The large mismatch between the resonance wavelength, $\lambda_{\rm p} \approx 4.9\,\mu{\rm m}$, and the size of the graphene nanodisk, $D=50\,{\rm nm}$, allows us to analyze its optical response in the electrostatic limit, using the plasmon wave function (PWF) formalism^{55,69-73} (see the Supporting Information). Within this framework, and neglecting any polarization perpendicular to the nanodisk due to the two-dimensional character of graphene, we can describe the response associated with the lowest order dipole plasmon resonance of the nanodisk using the following scalar polarizability.

$$\alpha(\omega) = \frac{D^3 \zeta_1^2}{-1/\eta_1 - i\omega D/\sigma(\omega)}.$$
 (4)

Here, η_1 and ζ_1 are two parameters whose values are determined solely by nanostructure shape, and therefore are independent of D, $E_{\rm F}$, and γ . For a given nanostructure shape, these parameters can be calculated from the fitting of the above polarizability to the corresponding results obtained from the numerical solution of Maxwell's equations using the FEM approach. In the case of a nanodisk, they take the values $\eta_1 = -0.0728$ and $\zeta_1 = 0.8508^{73}$ (see Figure S1 in the Supporting Information). By combining Eq. (3) with Eq. (4), we obtain the following analytical expression for the frequency of the plasmon resonance (see the Supporting Information for more details)

$$\omega_{\rm p} = \frac{e/\hbar}{\sqrt{-\pi\eta_1}} \sqrt{\frac{E_{\rm F}}{D}},\tag{5}$$

which reveals its dependence on both $E_{\rm F}$ and D.

The PWF formalism also states that the induced charge density associated with the dipole plasmon of the nanodisk, which is proportional to the corresponding PWF, depends exclusively on the shape of the nanostructure. ^{70,74,75} Therefore, we can parametrize it as $\rho(\theta,\phi) = N\rho_1(\theta,\phi)$, where $\rho_1(\theta,\phi) = R(\theta)\cos\phi$ is the PWF of the lowest order dipole plasmon of the nanodisk, $\theta = \sqrt{x^2 + y^2}/D$ is the normalized radial coordinate, ϕ is the

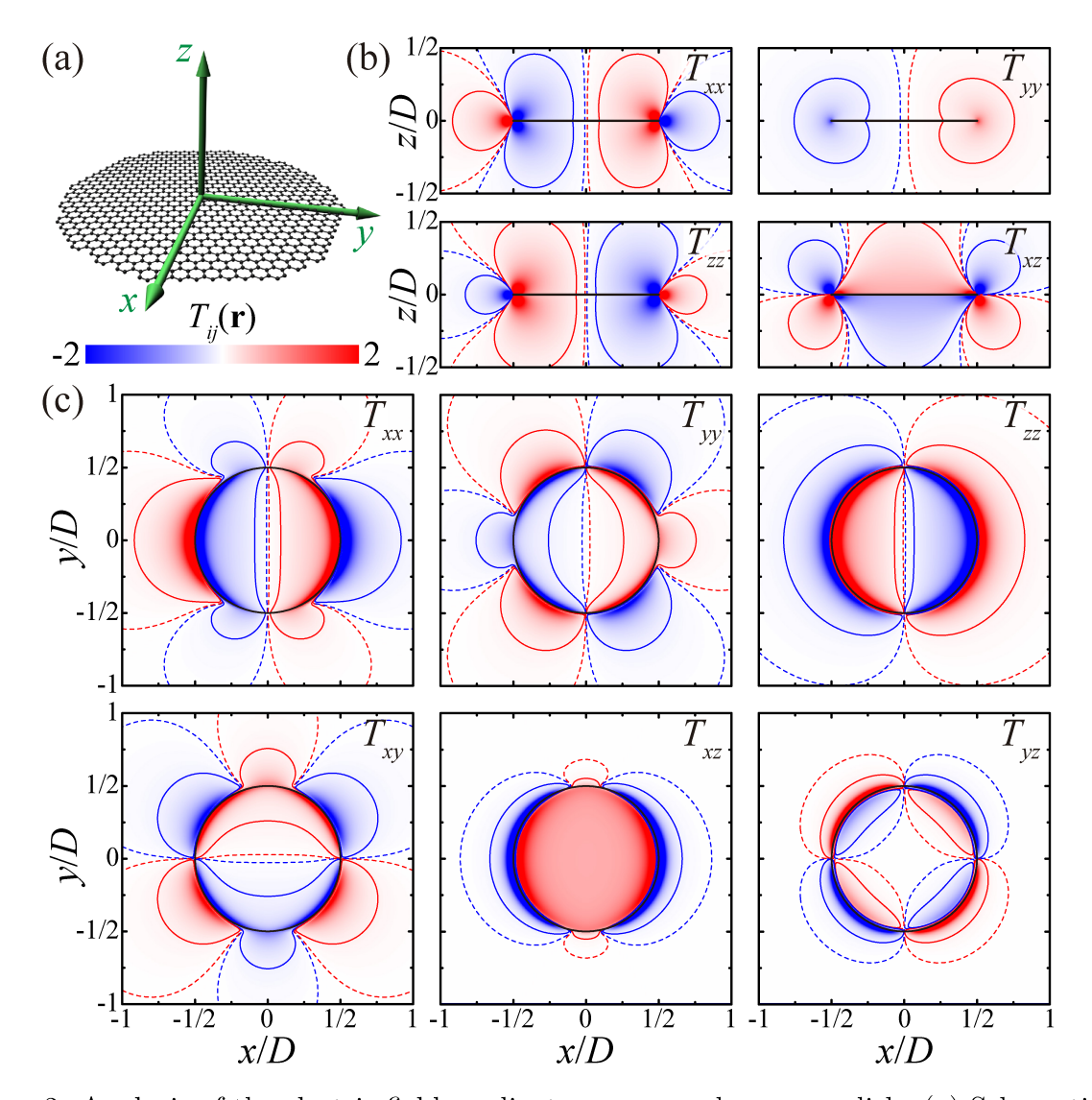


Figure 2: Analysis of the electric field gradient near a graphene nanodisk. (a) Schematics of the system under study. (b) Different components of $T_{ij}(\mathbf{r})$ plotted on the xz plane. (c) Same as (b), but for a plane parallel to the nanodisk a distance z = 0.02D above it. In all of the plots, the dashed and solid red contours delimit the regions in which $T_{ij}(\mathbf{r})$ is, respectively, larger than 0.01 and 0.1, while the corresponding dashed and solid blue contours signal the regions for which T_{ij} is below -0.01 and -0.1. The edge of the nanodisk is indicated by the solid black contours.

azimuthal angle, and N is a normalization constant defined as $N = |\alpha(\omega_p)E_0|/D^3\zeta_1$, which ensures that $\rho(\theta, \phi)$ produces the correct dipole amplitude for E_0 . The cosine term arises from the dipolar character of the plasmon mode, while the radial part $R(\theta)$ can be extracted from a fitting to the FEM solution of Maxwell's equations, 70,74,75 which results in the following expression

$$R(\theta) = C\theta \left(1 + \frac{e^{-5(1-2\theta)}}{4\sqrt{1-2\theta}} \right),\,$$

with C being a normalization constant (see the Supporting Information for more details). Then, using $\rho(\theta, \phi)$ in combination with Coulomb's law, we obtain the following expression for the normalized components of the electric field gradient produced by the nanodisk at a certain position \mathbf{r}

$$\frac{\partial_i E_j(\mathbf{r})}{k_{\rm p} E_0} = \frac{\omega_{\rm p}}{\gamma} \frac{\lambda_{\rm p}}{D} T_{ij}(\mathbf{r}). \tag{6}$$

This expression shows that the field gradient is proportional to: (i) the quality factor of the plasmon resonance $\omega_{\rm p}/\gamma$, (ii) the mismatch between the resonance wavelength $\lambda_{\rm p}=2\pi c/\omega_{\rm p}$ and the nanostructure diameter D, and (iii) a geometric factor that is independent of D, $E_{\rm F}$ and γ , defined as

$$T_{ij}(\mathbf{r}) = \frac{-\eta_1 \zeta_1}{2\pi} \int_0^{\frac{1}{2}} d\theta \, \theta R(\theta) \int_0^{2\pi} d\phi \frac{\cos \phi}{h^3} \left[\delta_{ij} - 3 \frac{h_i h_j}{h^2} \right],$$

with $\mathbf{h} = \mathbf{r}/D - \theta(\hat{\mathbf{x}}\cos\phi + \hat{\mathbf{y}}\sin\phi)$. Therefore, once $T_{ij}(\mathbf{r})$ is calculated, we can use Eq. (6) to predict the enhancement of the electric field gradient produced by any graphene nanodisk with arbitrary D, $E_{\rm F}$, and γ . This analytical approach can be generalized to other graphene nanostructures with different shapes, including graphene nanoribbons.⁷³ To that end, it is necessary to obtain the corresponding values of η_1 and ζ_1 , as well as to compute $T_{ij}(\mathbf{r})$ by using the proper charge density profile.^{70,76} Furthermore, by differentiating Eq. (6) the pertinent number of times, this approach can be also employed to calculate the enhancement of higher order multipolar transitions, which are proportional to higher order derivatives. The resulting expression for the nth order derivative scale as $(\lambda_{\rm p}/D)^n$, with n=1 for the

quadrupole, n=2 for the octupole, etc.

Figure 2 shows the different nonzero components of $T_{ij}(\mathbf{r})$ calculated in the vicinity of an arbitrary graphene nanodisk, as the one depicted in panel (a). The results for the xzplane are shown in panel (b), while those calculated at a plane parallel to the nanodisk a distance z = 0.02D above it are displayed in panel (c). In all cases, we use red contours to signal the regions for which $T_{ij}(\mathbf{r})$ is larger than 0.01 (red dashed curves) or 0.1 (red solid curves), whereas blue contours delimit the regions for which this quantity is below -0.01(blue dashed curves) or -0.1 (blue solid curves). From its definition, $T_{ij}(\mathbf{r})$ is symmetric under the exchange of the indices i and j. This is because Eq. (6) calculates the field gradient induced by the nanodisk without including that produced by the illuminating plane wave. The inclusion of the latter adds a contribution $\partial_z E_x(\mathbf{r})/k_{\rm p}E_0 = ie^{ik_{\rm p}z}$, which is negligible for the systems under study (see the results of Figure 1). Following Eq. (6), we can multiply the values of $T_{ij}(\mathbf{r})$ shown in Figure (2) by the factor $(\omega_p/\gamma)(\lambda_p/D)$ to calculate the enhancement of the electric field gradient generated by an arbitrary graphene nanodisk. As shown in Figure S3 in the Supporting Information, the predictions of this analytical model, based on the PWF formalism, are in excellent agreement with the FEM calculations. Furthermore, Eq. (6) provides valuable insight into the effect that the different characteristics of the graphene nanostructure have on the enhancement of the field gradient. In particular, it confirms that lower levels of losses and smaller diameters lead to larger field gradients. This is justified by the fact that the confinement of the electric field produced by the plasmon resonance is proportional to D^{-1} , so smaller disks lead to higher levels of confinement, and therefore force the field to decay in smaller distances. It also shows that, since $\omega_p \lambda_p = 2\pi c$, the enhancement of the field gradient does not depend directly on the resonance frequency and, therefore, can be tuned to the desired frequency by choosing an appropriate combination of values for $E_{\rm F}$ and D following Eq. (5).

The shape of the graphene nanoisland is another aspect that can influence its performance. In principle, vertices and other sharp features in the shape of the nanoisland are

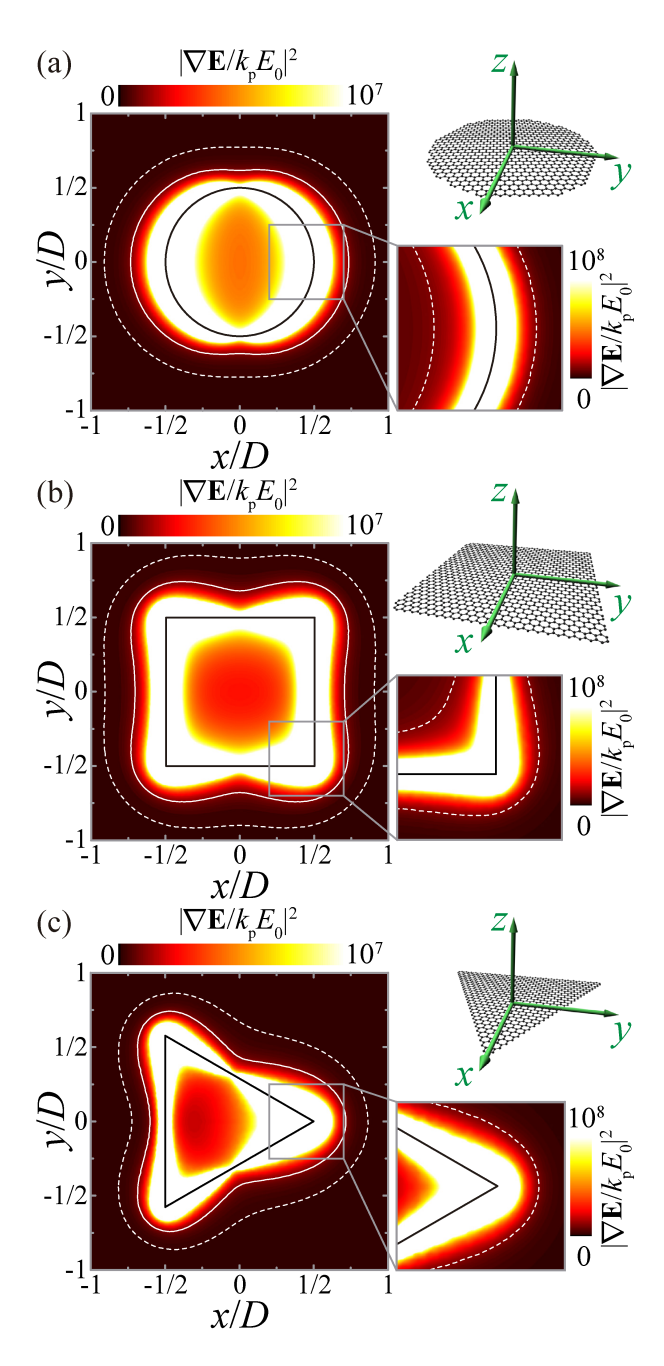


Figure 3: Analysis of the effect of the nanostructure shape on the near field response. (a)-(c) Enhancement of field gradient intensity for three different graphene nanoislands, as shown in the upper-right insets, calculated in a plane parallel to and a distance z = 0.02D above them. In all of the cases, we assume $D = 50 \,\mathrm{nm}$ and $E_{\mathrm{F}} = 0.5 \,\mathrm{eV}$. The nanostructures are illuminated with a plane wave propagating along the z axis and polarized along the x axis, which oscillates at a frequency resonant with the lowest order dipole plasmon of the corresponding structure. In the three panels, the dashed and solid white contours signal the regions for which the enhancement of the field gradient is larger than 10^5 and 10^6 , respectively, while the black contours indicate the boundary of the nanoisland. The lower insets show a zoom of the regions with intense field enhancement. In this case, the dashed white contours indicate the region for which the enhancement is above 10^7 .

expected to provide an extra enhancement of the field gradient. ⁷⁷ To explore this effect, we compare the response of a graphene nanodisk of diameter D with those of a nanosquare of lateral size D, and an equilateral nanotriangle with height D, as shown in the upper-right insets of Figure 3. In all cases, we choose $D=50\,\mathrm{nm}$ and $E_\mathrm{F}=0.5\,\mathrm{eV}$. Panels (a)-(c) show the resulting enhancement of the field gradient calculated in a plane parallel to the nanoislands situated a distance z = 0.02D above them. Each of these calculations is performed assuming illumination with a plane wave propagating along the z axis and polarized along the x axis, with a frequency resonant with the lowest order dipole plasmon of the corresponding nanostructure: $\hbar\omega_{\rm p}=0.251\,{\rm eV}$ for the disk, $\hbar\omega_{\rm p}=0.221\,{\rm eV}$ for the square, and $\hbar\omega_{\rm p}=0.212\,{\rm eV}$ for the nanotriangle (see Figure S4 in the Supporting Information for the extinction spectra of these nanostructures). In all of the plots, we use dashed and solid curves to delimit the regions for which the enhancement is above 10⁵ and 10⁶, respectively, and a black solid contour to signal the boundary of the corresponding nanoisland. Examining these results, we observe that, around the vertices of the nanosquare and the nanotriangle, the field gradient enhancement takes larger values than in other parts of these nanostructures, which can be inferred from the larger distance between the nanoisland boundary and the white solid contour. This is especially evident at the rightmost vertex of the nanotriangle, due to the large charge accumulation produced by the plasmon oscillation, as shown in Figure S5 of the Supporting Information. However, taking a closer look at these zones, we realize that the enhancement pattern is not significantly different from that produced by the nanodisk. We attribute this to the fact that the extra enhancement provided by the sharp features is very localized near the nanostructure edge, as can be seen in the lower-right insets, and therefore does not have a large effect on the overall enhancement (notice that, in this case, the dashed white contours delimit the region with enhancement above 10^7). It is important to remark that, very close to the nanostructure, for distances comparable to $v_{\rm F}/\omega$, we expect corrections of the response arising from finite-size and nonlocal effects, as well as from the atomic structure of the graphene edge. 78,79 These corrections will tend to reduce the values of the gradient enhancement.⁵³ Figure S6 of the Supporting Information shows the evolution of the gradient enhancement as z becomes larger for the graphene nanostructures discussed in Figure 3. Although, as expected, the maximum values of the enhancement decrease with z, the region for which it is larger than 10^5 remains almost unchanged, even for z = 0.2D.

Although a single graphene nanoisland is an adequate geometry to understand the fundamental mechanisms behind the plasmonic enhancement of the electric field gradient, it is not an ideal platform for an experimental realization of the concepts proposed here. Any realistic implementation requires extended geometries capable of maximizing the spatial overlap with the quadrupolar emitters. An interesting possibility, which we investigate in the following, is an array of graphene nanoribbons, as the one shown in Figure 4(a). These structures have been shown to support localized plasmons with properties similar to those of nanodisks when illuminated with light polarized across their length. 80,81 However, in contrast to graphene nanoislands, they can be electrically doped using metallic contacts situated far from the working region, which relaxes the fabrication requirements. ⁶³ In order to explore this possibility, we calculate the near field response of an array of nanoribbons of width $D = 50 \,\mathrm{nm}$, separated by a center-to-center distance a = 1.4D. We assume the structure to be illuminated with a plane wave propagating along the z axis and polarized across the ribbons (i.e. along the x axis), with a frequency resonant with the lowest order dipole mode of the ribbons, $\hbar\omega_{\rm p}=0.224\,{\rm eV}.$ The corresponding results for the enhancement of the field gradient intensity are plotted in Figure 4(b). Clearly, values above 10⁵ (dashed white contours) are predicted over almost an entire strip of width D around the array. Closer to the edges of the ribbons, the enhancement reaches values beyond 10⁶, as indicated by the solid white contours. These results confirm that the performance of the nanoribbon array is similar to that of the individual nanoislands, but with the advantage that the enhancement shown in Figure 4(b) is maintained at any position along the ribbon length, due to the translational invariance of the system. It is important to note that, in principle, such symmetry can also constitute a drawback, since it results in the vanishing of all of the components of the field

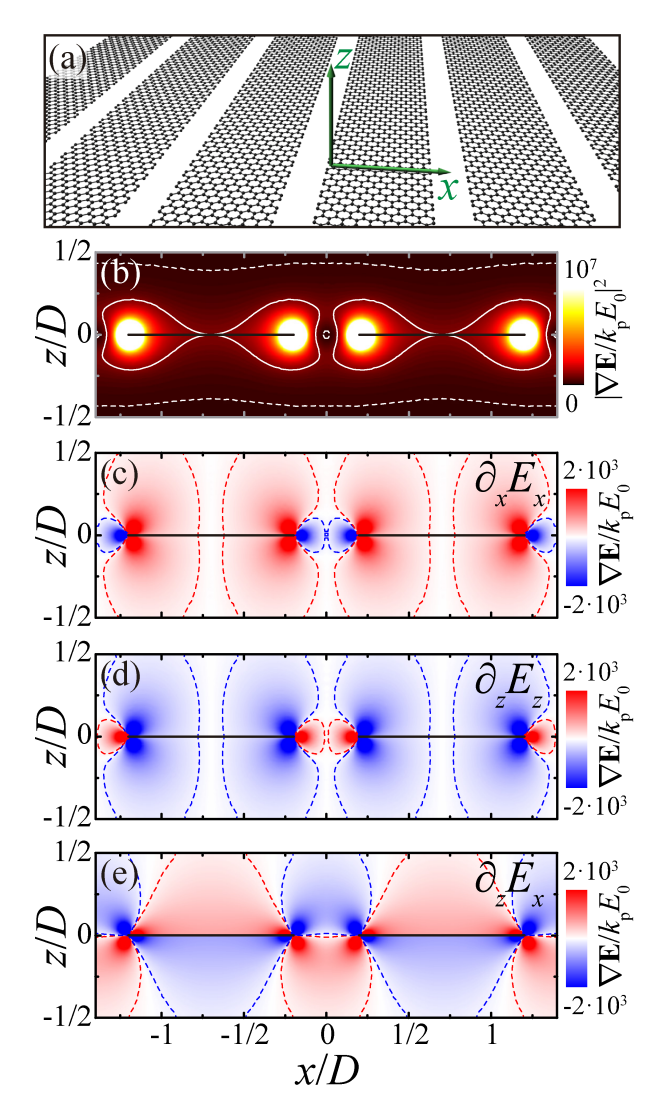


Figure 4: Field gradient enhancement produced by a ribbon array. (a) Schematics of the system under study, composed of a periodic array of ribbons with lateral size $D=50\,\mathrm{nm}$, separated by a center-to-center distance a=1.4D, and a Fermi level $E_{\mathrm{F}}=0.5\,\mathrm{eV}$. The array is illuminated with a plane wave propagating along the z axis and polarized along the x axis, resonant with the lowest order dipole mode of the ribbons. (b) Enhancement of the field gradient intensity around the ribbon array. The dashed and solid white contours signal the regions for which $|\nabla \mathbf{E}/k_{\mathrm{p}}E_{0}|^{2}$ is larger than 10^{5} and 10^{6} , respectively. (c)-(e) Enhancement of the xx (c), zz (d), and zx (e) components of the field gradient. The red and blue dashed contours delimit the regions in which the components of $\nabla \mathbf{E}/k_{\mathrm{p}}E_{0}$ are, respectively, above 100 and below -100, while the solid black lines indicate the position of the nanoribbon.

gradient involving the y axis. However, the remaining components are sufficient to allow for the excitation of any arbitrary quadrupolar transition. Panels (c), (d), and (e) show, respectively, the enhancement of the xx, zz, and zx components of the field gradient. Note that xz (not shown) is almost identical to the zx component, since the only difference between them is the almost negligible contribution produced by the illuminating plane wave. In these plots, we use red and blue dashed contours to indicate the regions for which the enhancement of the field gradient amplitude reaches values above 100 and below -100, respectively. These results confirm that both diagonal and off-diagonal components of the field gradient take large values around the nanoribbons.

Therefore, the nanoribbon array provides an efficient platform to enhance quadrupolar transitions. In particular, we envision a device in which the emitters flow through the gaps between the nanoribbons, thus providing a large region for them to interact with the strong field gradient produced by the plasmons supported by the array. If necessary, the interaction region can be further enlarged by stacking several layers of nanoribbon arrays along the z axis. To analyze the efficiency of the proposed platform in a systematic way, and to characterize the effect of the different design parameters, we introduce a figure of merit defined as

FOM =
$$\frac{1-f}{A} \int dS \frac{|\nabla \mathbf{E}(\mathbf{r})|^2}{|k_p E_0|^2}$$
.

Here, f = D/a is the graphene filling fraction of the array, and therefore the factor 1 - f takes into account how efficiently the emitters flow through the array, while the surface integral is performed over the rectangular area A = 0.9(a - D)D, indicated in the inset of Figure 5(b), which avoids the nonphysical results obtained exactly at the ribbon edges. The defined FOM quantifies the spatially averaged enhancement of the field gradient intensity that an emitter experiences as it flows through the array.

Figure 5(a) analyzes the effect of D and $E_{\rm F}$ on the FOM for different arrays of nanoribbons, all of them with period a=1.4D. The size of the dots encodes the value of the FOM,

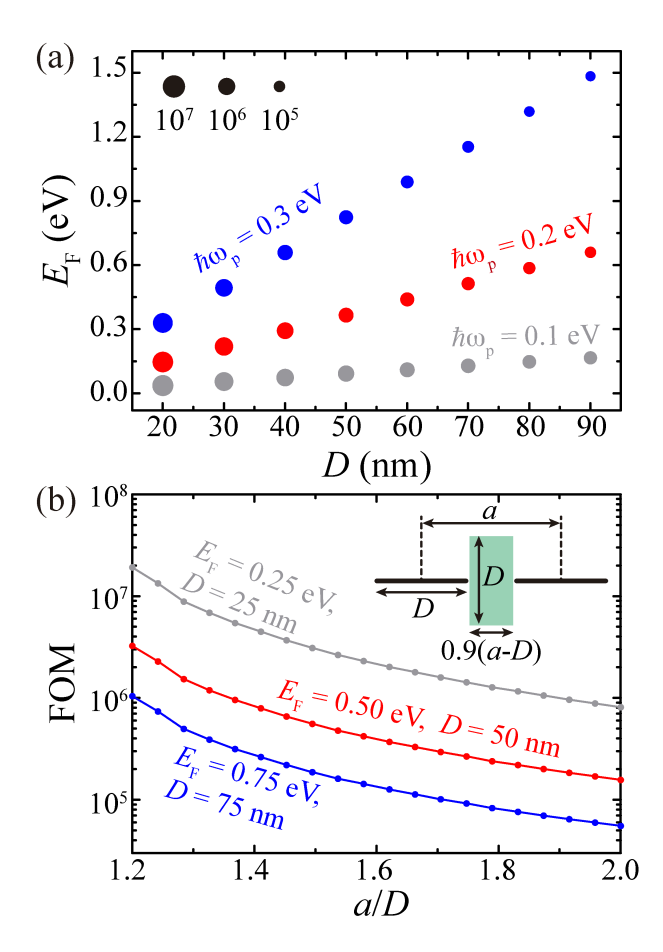


Figure 5: Effect of geometry and Fermi level on the performance of the ribbon array. (a) Analysis of the FOM defined in the text for a ribbon array with a = 1.4D. Gray, red, and blue dots indicate combinations of $E_{\rm F}$ and D that result in a plasmon resonance of energy 0.1, 0.2, and 0.3 eV, respectively. The size of the dots is proportional to the value of the FOM, as indicated by upper left legend. (b) FOM as a function of a/D for the three different combinations of $E_{\rm F}$ and D indicated by the labels. The inset shows the schematics of the array geometry indicating the region over which the enhancement of the field gradient is averaged to calculate the FOM (green area).

as explained by the legend in the upper-left corner, while their position indicates the values of D and $E_{\rm F}$. We use gray, red, and blue dots to label combinations of D and $E_{\rm F}$ that produce a plasmon resonance of energy 0.1, 0.2, and 0.3 eV, respectively. As in the case of the nanodisk (see Eq. (5)), these sets of dots lie on top of straight lines with a slope proportional to $\omega_{\rm p}^2$, with the proportionality constant only dependent on a/D. This highlights the extraordinary tunability of these nanostructures. Examining these results, we observe that, for a given target frequency, the largest FOM is obtained for the systems with the smallest D, and, consequently, $E_{\rm F}$. This is the expected trend, since a smaller D provides a larger mismatch with the resonance wavelength. A similar behavior is observed in the results shown in panel (b), where we analyze the FOM as a function of a/D for three different combinations of D and $E_{\rm F}$, as indicated by the labels. In all of the cases, the value of the FOM increases as a/D is reduced, which is a direct consequence of the larger field confinement provided by arrays with smaller gaps. All of these results show that the most advantageous geometries are those with small nanoribbons separated by small gaps. However, this trend is expected to break down for sufficiently small D and a, when finite-size and nonlocal effects become significant. 53,78,79

Conclusions

In summary, we have shown that the plasmons of graphene nanoislands give rise to extraordinary electric field gradients, which, together with their electrical tunability, makes these systems ideal platforms to enhance the quadrupolar transitions of quantum emitters placed in their vicinity. Using rigorous numerical solutions of Maxwell's equations, together with an analytic electrostatic approach based on the plasmon wave function formalism, we have analyzed how the different geometric and material characteristics of the graphene nanostructures influence the field gradient they produce. We have found that, while size has a strong effect on the field gradient, with smaller structures producing larger values, the shape only has a local impact on the value of gradient near the edges of the nanostructure, not significantly altering its overall response. Furthermore, we have derived a universal expression for the electric field gradient generated by a nanodisk of arbitrary size, Fermi energy, and damping, which provides valuable insight on the physical mechanisms that produce the field gradient. We have also investigated the performance of arrays of graphene nanoribbons as a potential platform for the experimental verification of our predictions. These systems produce field gradients comparable to those of single nanoislands with less demanding fabrication standards, while simultaneously allowing for the maximization of the interaction with the quadrupolar emitters. The results of this work show the extraordinary ability of graphene nanostructures to generate large electric field gradients that can be exploited to enhance quadrupolar transitions of quantum emitters, thus having a potential impact on the development of new applications in sensing, light emission, and quantum information processing.

Acknowledgement

This work has been sponsored by the National Science Foundation (Grant ECCS-1710697). We would like to thank the UNM Center for Advanced Research Computing, supported in part by the National Science Foundation, for providing the high performance computing resources used in this work.

Supporting Information Available

Detailed description of the theoretical methods used in this work. Comparison of the PWF formalism with the rigorous solution of Maxwell's equations. Extinction spectrum and induced charge maps for the nanostructures of Figure 3. Plots showing the gradient enhancement of the nanostructures of Figure 3 calculated at larger distances from their surface.

References

- (1) Barron, L. D.; Gray, C. G. The multipole interaction Hamiltonian for time dependent fields. J. Phys. A 1973, 6, 59.
- (2) Craig, D.; Thirunamachandran, T. Molecular Quantum Electrodynamics: An Introduction to Radiation-molecule Interactions; Dover Books on Chemistry Series; Dover Publications, 1984.
- (3) Jackson, J. D. Classical Electrodynamics; Wiley: New York, 1999.
- (4) Messiah, A. Quantum Mechanics; North-Holland: New York, 1966.
- (5) Sayer, B.; Wang, R.; Jeannet, J. C.; Sassi, M. Absorption measurements of quadrupole transition probabilities 6S-nD in caesium vapour. J. Phys. B: At. Mol. Phys. 1971, 4, L20.
- (6) Tojo, S.; Hasuo, M.; Fujimoto, T. Absorption Enhancement of an Electric Quadrupole Transition of Cesium Atoms in an Evanescent Field. *Phys. Rev. Lett.* **2004**, *92*, 053001.
- (7) Tojo, S.; Fujimoto, T.; Hasuo, M. Precision measurement of the oscillator strength of the cesium $6\,^2S_{1/2} \rightarrow 5\,^2D_{5/2}$ electric quadrupole transition in propagating and evanescent wave fields. *Phys. Rev. A* **2005**, *71*, 012507.
- (8) Dodson, C. M.; Zia, R. Magnetic dipole and electric quadrupole transitions in the trivalent lanthanide series: Calculated emission rates and oscillator strengths. *Phys. Rev. B* 2012, 86, 125102.
- (9) Enzonga Yoca, S.; Quinet, P. Radiative Decay Rates for Electric Dipole, Magnetic Dipole and Electric Quadrupole Transitions in Triply Ionized Thulium (Tm IV). Atoms 2017, 5, 28.

- (10) Camy-Peyret, C.; Flaud, J.-M.; Delbouille, L.; Roland, G.; Brault, J. W.; Testerman, L. Quadrupole transitions of the 1←0 band of N₂ observed in a high resolution atmospheric spectrum. J. Phys. Lett. 1981, 42, 279–283.
- (11) Tipping, R. H.; Brown, A.; Ma, Q.; Hartmann, J. M.; Boulet, C.; Liévin, J. Collision-induced absorption in the N₂ fundamental band of CH4. I. Determination of the quadrupole transition moment. J. Chem. Phys. 2001, 115, 8852–8857.
- (12) Li, W.; Pohl, T.; Rost, J. M.; Rittenhouse, S. T.; Sadeghpour, H. R.; Nipper, J.; Butscher, B.; Balewski, J. B.; Bendkowsky, V.; Löw, R.; Pfau, T. A Homonuclear Molecule with a Permanent Electric Dipole Moment. Science 2011, 334, 1110–1114.
- (13) Cheng, C.-F.; Sun, Y. R.; Pan, H.; Wang, J.; Liu, A.-W.; Campargue, A.; Hu, S.-M. Electric-quadrupole transition of H₂ determined to 10⁻⁹ precision. *Phys. Rev. A* 2012, 85, 024501.
- (14) Hu, S.-M.; Pan, H.; Cheng, C.-F.; Sun, Y. R.; Li, X.-F.; Wang, J.; Campargue, A.; Liu, A.-W. The $V=3\leftarrow 0$ S(0)-S(3) Electric Quadrupole Transitions of H₂ near 0.8 μ m. Astrophys. J. **2012**, 749, 76.
- (15) Maier, S. A. Plasmonics: Fundamentals and Applications; Springer: New York, 2007.
- (16) Halas, N. J.; Lal, S.; Chang, W.; Link, S.; Nordlander, P. Plasmons in strongly coupled metallic nanostructures. *Chem. Rev.* **2011**, *111*, 3913–3961.
- (17) Álvarez-Puebla, R. A.; Liz-Marzán, L. M.; García de Abajo, F. J. Light concentration at the nanometer scale. *J. Phys. Chem. Lett.* **2010**, *1*, 2428–2434.
- (18) Ciracì, C.; Hill, R. T.; Mock, J. J.; Urzhumov, Y.; Fernández-Domínguez, A. I.; Maier, S. A.; Pendry, J. B.; Chilkoti, A.; Smith, D. R. Probing the ultimate limits of plasmonic enhancement. *Science* 2012, 337, 1072–1074.

- (19) Kneipp, K.; Kneipp, H.; Itzkan, I.; Dasari, R. R.; Feld, M. S. Ultrasensitive Chemical Analysis by Raman Spectroscopy. *Chem. Rev.* **1999**, *99*, 2957–2976.
- (20) Moskovits, M. Surface-enhanced Raman spectroscopy: a brief retrospective. *J. Raman Spectrosc.* **2005**, *36*, 485–496.
- (21) Haes, A. J.; Haynes, C. L.; McFarland, A. D.; Schatz, G. C.; Van Duyne, R. P.; Zou, S. Plasmonic materials for surface-enhanced sensing and spectroscopy. MRS Bulletin 2005, 30, 368–375.
- (22) Kundu, J.; Le, F.; Nordlander, P.; Halas, N. J. Surface enhanced infrared absorption (SEIRA) spectroscopy on nanoshell aggregate substrates. *Chem. Phys. Lett.* **2008**, 452, 115–119.
- (23) Rodríguez-Lorenzo, L.; Álvarez-Puebla, R. A.; Pastoriza-Santos, I.; Mazzucco, S.; Stéphan, O.; Kociak, M.; Liz-Marzán, L. M.; García de Abajo, F. J. Zeptomol detection through controlled ultrasensitive surface-enhanced Raman scattering. J. Am. Chem. Soc. 2009, 131, 4616–4618.
- (24) Zhang, R.; Zhang, Y.; Dong, Z. C.; Jiang, S.; Zhang, C.; Chen, L. G.; Zhang, L.; Liao, Y.; Aizpurua, J.; Luo, Y.; Yang, J. L.; Hou, J. G. Chemical mapping of a single molecule by plasmon-enhanced Raman scattering. *Nature* **2013**, *498*, 82–86.
- (25) Aouani, H.; Šípová, H.; Rahmani, M.; Navarro-Cía, M.; Hegnerová, K.; Homola, J.; Hong, M.; Maier, S. A. Ultrasensitive broadband probing of molecular vibrational modes with multifrequency optical antennas. *ACS Nano* **2013**, *7*, 669–675.
- (26) Neubrech, F.; Huck, C.; Weber, K.; Pucci, A.; Giessen, H. Surface-Enhanced Infrared Spectroscopy Using Resonant Nanoantennas. *Chem. Rev.* **2017**, *117*, 5110–5145.
- (27) Lozano, G.; Louwers, D. J.; Rodriguez, S. R. K.; Murai, S.; Jansen, O. T. A.; Verschu-

- uren, M. A.; Gomez Rivas, J. Plasmonics for solid-state lighting: enhanced excitation and directional emission of highly efficient light sources. *Light Sci. Appl.* **2013**, 2, e241.
- (28) Zhou, W.; Dridi, M.; Suh, J. Y.; Kim, C. H.; Co, D. T.; Wasielewski, M. R.; Schatz, G. C.; Odom, T. W. Lasing action in strongly coupled plasmonic nanocavity arrays. *Nat. Nanotechnol.* **2013**, *8*, 506–511.
- (29) Yang, A.; Odom, T. W. Breakthroughs in Photonics 2014: Advances in Plasmonic Nanolasers. *IEEE Photonics Journal* **2015**, *7*, 1–6.
- (30) Liu, K.; Li, N.; Sadana, D. K.; Sorger, V. J. Integrated nanocavity plasmon light sources for on-chip optical interconnects. *ACS Photonics* **2016**, *3*, 233–242.
- (31) Grosjean, T.; Mivelle, M.; Baida, F. I.; Burr, G. W.; Fischer, U. C. Diabolo Nanoantenna for Enhancing and Confining the Magnetic Optical Field. *Nano Lett.* **2011**, *11*, 1009–1013.
- (32) Monticone, F.; Alu, A. The quest for optical magnetism: from split-ring resonators to plasmonic nanoparticles and nanoclusters. J. Mater. Chem. C 2014, 2, 9059–9072.
- (33) Verre, R.; Yang, Z. J.; Shegai, T.; Käll, M. Optical Magnetism and Plasmonic Fano Resonances in Metal-Insulator-Metal Oligomers. *Nano Lett.* **2015**, *15*, 1952–1958.
- (34) Zurita-Sánchez, J. R.; Novotny, L. Multipolar interband absorption in a semiconductor quantum dot. II. Magnetic dipole enhancement. J. Opt. Soc. Am. B 2002, 19, 2722– 2726.
- (35) Oulton, R. F.; Sorger, V. J.; Zentgraf, T.; Ma, R. M.; Gladden, C.; Dai, L.; Bartal, G.; Zhang, X. Plasmon lasers at deep subwavelength scale. *Nature* **2009**, *461*, 629–632.
- (36) Taminiau, T. H.; Karaveli, S.; van Hulst, N. F.; Zia, R. Quantifying the magnetic nature of light emission. *Nat. Commun.* **2012**, *3*, 979.

- (37) Mivelle, M.; Grosjean, T.; Burr, G. W.; Fischer, U. C.; Garcia-Parajo, M. F. Strong Modification of Magnetic Dipole Emission through Diabolo Nanoantennas. *ACS Photonics* **2015**, *2*, 1071–1076.
- (38) Kasperczyk, M.; Person, S.; Ananias, D.; Carlos, L. D.; Novotny, L. Excitation of Magnetic Dipole Transitions at Optical Frequencies. *Phys. Rev. Lett.* **2015**, *114*, 163903.
- (39) Baranov, D. G.; Savelev, R. S.; Li, S. V.; Krasnok, A. E.; Alù, A. Modifying magnetic dipole spontaneous emission with nanophotonic structures. *Laser Photon. Rev.* 2017, 11, 1600268.
- (40) Toftegaard, R.; Arnbjerg, J.; Daasbjerg, K.; Ogilby, P.; Dmitriev, A.; Sutherland, D.; Poulsen, L. Metal-Enhanced 1270-nm Singlet Oxygen Phosphorescence. Angew. Chem. Int. Ed 2008, 47, 6025–6027.
- (41) Manjavacas, A.; Fenollosa, R.; Rodriguez, I.; Jimenez, M. C.; Miranda, M.; Meseguer, F. Magnetic Light and Forbidden Photochemistry: The Case of Singlet Oxygen. J. Mater. Chem. C 2017, 5, 11824–11831.
- (42) Alabastri, A.; Yang, X.; Manjavacas, A.; Everitt, H. O.; Nordlander, P. Extraordinary light-induced local angular momentum near metallic nanoparticles. ACS Nano 2016, 10, 4835–4846.
- (43) Moskovits, M.; DiLella, D. P. Intense quadrupole transitions in the spectra of molecules near metal surfaces. *J. Chem. Phys.* **1982**, *77*, 1655–1660.
- (44) Klimov, V. V.; Ducloy, M. Quadrupole transitions near an interface: General theory and application to an atom inside a planar cavity. *Phys. Rev. A* **2005**, *72*, 043809.
- (45) Deguchi, K.; Okuda, M.; Iwamae, A.; Nakamura, H.; Sawada, K.; Hasuo, M. Simulation of Electric Quadrupole and Magnetic Dipole Transition Efficiencies in Optical Near Fields Generated by a Subwavelength Slit Array. J. Phys. Soc. Jpn. 2009, 78, 024301.

- (46) Kern, A. M.; Martin, O. J. F. Strong enhancement of forbidden atomic transitions using plasmonic nanostructures. *Phys. Rev. A* **2012**, *85*, 022501.
- (47) Filter, R.; Mühlig, S.; Eichelkraut, T.; Rockstuhl, C.; Lederer, F. Controlling the dynamics of quantum mechanical systems sustaining dipole-forbidden transitions via optical nanoantennas. *Phys. Rev. B* **2012**, *86*, 035404.
- (48) Heeres, R. W.; Zwiller, V. Subwavelength Focusing of Light with Orbital Angular Momentum. *Nano Lett.* **2014**, *14*, 4598–4601.
- (49) Yannopapas, V.; Paspalakis, E. Giant enhancement of dipole-forbidden transitions via lattices of plasmonic nanoparticles. *J. Mod. Opt.* **2015**, *62*, 1435–1441.
- (50) Zurita-Sánchez, J. R.; Novotny, L. Multipolar interband absorption in a semiconductor quantum dot. I. Electric quadrupole enhancement. J. Opt. Soc. Am. B 2002, 19, 1355– 1362.
- (51) Sun, M.; Zhang, Z.; Chen, L.; Sheng, S.; Xu, H. Plasmonic Gradient Effects on High Vacuum Tip-Enhanced Raman Spectroscopy. *Adv. Optical Mater.* **2014**, *2*, 74–80.
- (52) Meng, L.; Yang, Z.; Chen, J.; Sun, M. Effect of Electric Field Gradient on Subnanometer Spatial Resolution of Tip-enhanced Raman Spectroscopy. Sci. Rep. 2015, 5, 9240.
- (53) Koppens, F. H. L.; Chang, D. E.; García de Abajo, F. J. Graphene plasmonics: A platform for strong light-matter interactions. *Nano Lett.* **2011**, *11*, 3370–3377.
- (54) Grigorenko, A. N.; Polini, M.; Novoselov, K. S. Graphene plasmonics. *Nat. Photon.* **2012**, *6*, 749–758.
- (55) García de Abajo, F. J. Graphene plasmonics: Challenges and opportunities. *ACS Photon.* **2014**, *1*, 135–152.

- (56) Chen, J.; Badioli, M.; Alonso-González, P.; Thongrattanasiri, S.; Huth, F.; Osmond, J.; Spasenović, M.; Centeno, A.; Pesquera, A.; Godignon, P.; Zurutuza Elorza, A.; Camara, N.; García de Abajo, F. J.; Hillenbrand, R.; Koppens, F. H. L. Optical nanoimaging of gate-tunable graphene plasmons. *Nature* 2012, 487, 77–81.
- (57) Fei, Z.; Rodin, A. S.; Andreev, G. O.; Bao, W.; McLeod, A. S.; Wagner, M.; Zhang, L. M.; Zhao, Z.; Thiemens, M.; Dominguez, G.; Fogler, M. M.; Neto, A. H. C.; Lau, C. N.; Keilmann, F.; Basov, D. N. Gate-tuning of graphene plasmons revealed by infrared nano-imaging. *Nature* 2012, 487, 82–85.
- (58) Soto Lamata, I.; Alonso-González, P.; Hillenbrand, R.; Nikitin, A. Y. Plasmons in Cylindrical 2D Materials as a Platform for Nanophotonic Circuits. *ACS Photonics* **2015**, 2, 280–286.
- (59) Nikitin, A. Y.; Alonso-González, P.; Vélez, S.; Mastel, S.; Centeno, A.; Pesquera, A.; Zurutuza, A.; Casanova, F.; Hueso, L. E.; Koppens, F. H. L.; Hillenbrand, R. Realspace mapping of tailored sheet and edge plasmons in graphene nanoresonators. *Nat. Photonics* 2016, 10, 239.
- (60) Lin, X.; Rivera, N.; López, J. J.; Kaminer, I.; Chen, H.; Soljačić, M. Tailoring the energy distribution and loss of 2D plasmons. *New J. Phys.* **2016**, *18*, 105007.
- (61) Yan, H.; Li, X.; Chandra, B.; Tulevski, G.; Wu, Y.; Freitag, M.; Zhu, W.; Avouris, P.; Xia, F. Tunable infrared plasmonic devices using graphene/insulator stacks. *Nat. Nanotechnol.* 2012, 7, 330–334.
- (62) Fang, Z.; Wang, Y.; Schlather, A.; Liu, Z.; Ajayan, P. M.; García de Abajo, F. J.; Nordlander, P.; Zhu, X.; Halas, N. J. Active Tunable Absorption Enhancement with Graphene Nanodisk Arrays. Nano Lett. 2014, 14, 299–304.
- (63) Rodrigo, D.; Limaj, O.; Janner, D.; Etezadi, D.; García de Abajo, F. J.; Pruneri, V.;

- Altug, H. Mid-infrared plasmonic biosensing with graphene. Science **2015**, 349, 165–168.
- (64) Rivera, N.; Kaminer, I.; Zhen, B.; Joannopoulos, J. D.; Soljačić, M. Shrinking light to allow forbidden transitions on the atomic scale. *Science* **2016**, *353*, 263–269.
- (65) Bolotin, K. I.; Sikes, K. J.; Jiang, Z.; Klima, M.; Fudenberg, G.; Hone, J.; Kim, P.; Stormer, H. L. Ultrahigh electron mobility in suspended graphene. Sol. State Commun. 2008, 146, 351–355.
- (66) Dean, C. R.; Young, A. F.; Meric, I.; Lee, C.; Wang, L.; Sorgenfrei, S.; Watanabe, K.; Taniguchi, T.; Kim, P.; Shepard, K. L.; Hone, J. Boron nitride substrates for high-quality graphene electronics. *Nat. Nanotechnol.* **2010**, *5*, 722–726.
- (67) Banszerus, L.; Schmitz, M.; Engels, S.; Dauber, J.; Oellers, M.; Haupt, F.; Watanabe, K.; Taniguchi, T.; Beschoten, B.; Stampfer, C. Ultrahigh-mobility graphene devices from chemical vapor deposition on reusable copper. *Sci. Adv.* **2015**, *1*.
- (68) Jitrik, O.; Bunge, C. F. Transition Probabilities for Hydrogen-Like Atoms. *J. Phys. Chem. Ref. Data* **2004**, *33*, 1059–1070.
- (69) García de Abajo, F. J. Multiple excitation of confined graphene plasmons by single free electrons. *ACS Nano* **2013**, *7*, 11409–11419.
- (70) García de Abajo, F. J.; Manjavacas, A. Plasmonics in atomically thin materials. *Faraday Discuss.* **2015**, *178*, 87–107.
- (71) Silveiro, I.; Plaza Ortega, J. M.; García de Abajo, F. J. Plasmon wave function of graphene nanoribbons. *New J. Phys.* **2015**, *17*, 083013.
- (72) Zundel, L.; Manjavacas, A. Spatially resolved optical sensing using graphene nanodisk arrays. ACS Photonics 2017, 4, 1831–1838.

- (73) Yu, R.; Cox, J. D.; Saavedra, J. R. M.; García de Abajo, F. J. Analytical Modeling of Graphene Plasmons. *ACS Photonics* **2017**, *4*, 3106–3114.
- (74) Silveiro, I.; García de Abajo, F. J. Plasmons in inhomogeneously doped neutral and charged graphene nanodisks. *Appl. Phys. Lett.* **2014**, *104*, 131103.
- (75) Yu, R.; Manjavacas, A.; García de Abajo, F. J. Ultrafast radiative heat transfer. *Nat. Commun.* **2017**, *8*, 2.
- (76) Thongrattanasiri, S.; Silveiro, I.; García de Abajo, F. J. Plasmons in electrostatically doped graphene. *Appl. Phys. Lett.* **2012**, *100*, 201105.
- (77) Shibata, K.; Tojo, S.; Bloch, D. Excitation enhancement in electric multipole transitions near a nanoedge. *Opt. Express* **2017**, *25*, 9476–9489.
- (78) Thongrattanasiri, S.; Manjavacas, A.; García de Abajo, F. J. Quantum finite-size effects in graphene plasmons. *ACS Nano* **2012**, *6*, 1766–1775.
- (79) Thongrattanasiri, S.; García de Abajo, F. J. Optical Field Enhancement by Strong Plasmon Interaction in Graphene Nanostructures. *Phys. Rev. Lett.* **2013**, *110*, 187401.
- (80) Christensen, J.; Manjavacas, A.; Thongrattanasiri, S.; Koppens, F. H. L.; García de Abajo, F. J. Graphene plasmon waveguiding and hybridization in individual and paired nanoribbons. *ACS Nano* **2012**, *6*, 431–440.
- (81) Nikitin, A. Y.; Guinea, F.; García-Vidal, F. J.; Martín-Moreno, L. Edge and waveguide terahertz surface plasmon modes in graphene microribbons. *Phys. Rev. B* **2011**, *84*, 161407(R).

Graphical TOC Entry

